Revision 2

Immiscible-melt inclusions in corundum megacrysts: Microanalyses and geological implications

XI-SHENG XU[1,2]*, XIAO-MING CHEN[1], WILLIAM L. GRIFFIN[1,2], SUZANNE Y. O'REILLY[1,2], XI-SONG ZHANG[1], AND LI-HUI CHEN[1]

***Corresponding Author**: XI-SHENG XU

Xi-Sheng Xu: [1]State Key Laboratory for Mineral Deposits Research, School of Earth Sciences and Engineering, Nanjing University, Nanjing 210023, China; [2]ARC Centre of Excellence for Core to Crust Fluid Systems, Dept. Earth and Environmental Sciences, Macquarie University, NSW 2109, Australia

Email: xsxu@nju.edu.cn

Xiao-Ming Chen: [1]State Key Laboratory for Mineral Deposits Research, School of Earth Sciences and Engineering, Nanjing University, Nanjing 210023, China

Email: xmchen@nju.edu.cn

W. L. Griffin: [1]State Key Laboratory for Mineral Deposits Research, School of Earth Sciences and Engineering, Nanjing University, Nanjing 210023, China; [2]ARC Centre of Excellence for Core to Crust Fluid Systems, Dept. Earth and Environmental Sciences, Macquarie University, NSW 2109, Australia

Email: bill.griffin@mq.edu.au

S.Y. O'Reilly: [1]State Key Laboratory for Mineral Deposits Research, School of Earth Sciences and Engineering, Nanjing University, Nanjing 210023, China; [2]ARC Centre of Excellence for Core to Crust Fluid Systems, Dept. Earth and Environmental Sciences, Macquarie University, NSW 2109, Australia

Email: sue.oreilly@mq.edu.au

Xi-Song Zhang: [1]State Key Laboratory for Mineral Deposits Research, School of Earth Sciences and Engineering, Nanjing University, Nanjing 210023, China
Email: xisongzhang6@126.com
Li-Hui Chen: [1]State Key Laboratory for Mineral Deposits Research, School of Earth Sciences and Engineering, Nanjing University, Nanjing 210023, China
Email: chenlh@nju.edu.cn

Immiscible-melt inclusions in corundum megacrysts: Microanalyses and geological implications

XI-SHENG XU[1,2*], XIAO-MING CHEN[1], WILLIAM L. GRIFFIN[1,2], SUZANNE Y. O'REILLY[1,2], XI-SONG ZHANG[1], AND LI-HUI CHEN[1]

[1]*State Key Laboratory for Mineral Deposits Research, School of Earth Sciences and Engineering, Nanjing University, Nanjing 210023, China*

[2]*ARC Centre of Excellence for Core to Crust Fluid Systems, Dept. Earth and Environmental Sciences, Macquarie University, NSW 2109, Australia*

ABSTRACT

Controversies on the origin of zircon, corundum, titanomagnetite and quartz megacrysts in alkali basalts mostly reflect the lack of direct evidence of a "melt reservoir" required for their formation. Various mineral megacrysts are carried up by Cenozoic (mostly younger than 25 Ma) alkali basalts that extend more than 4000 km along eastern China. Here we report unusual inclusions in corundum megacrysts from Changle, and we attribute their origin to the existence of a FeO*-SiO_2-Al_2O_3-ZrO_2-rich melt. The inclusions, analyzed using electron microprobe

and Raman microscopy, may be divided into two types. Type I inclusions are dominated by glassy materials, may have a dark part in BSE images composed of quartz, corundum and an amorphous substance (AS-1), and a bright part in BSE images composed of baddeleyite and a second distinct amorphous substance (AS-2). Compared with AS-1, AS-2 has higher concentrations of ZrO_2 and FeO* but lower concentrations of Al_2O_3 and SiO_2. We argue that the formation temperature of type I inclusions is ~ 1200 °C, and the generation of their bright and dark parts in BSE images may be attributed to the coexistence of immiscible melts. Type II inclusions are composed of zircon, quartz and an amorphous substance (AS-3). Both types of inclusions might be derived from a similar parent melt, which is FeO*-SiO_2-Al_2O_3-ZrO_2-rich. New SIMS *in-situ* U-Pb ages of 18 Ma and 13-14 Ma for zircon inclusions suggest that the corundum megacrysts, occurring in basaltic host rocks distributed along the middle segment of the N-S-trending Tanlu fault zone, formed from precursor residual magmas related to underplating basalts stalled at the crust-mantle boundary, and were brought to the surface by entrainment in later basalts. This study provides new insights into the genesis of the corundum-related megacryst suite.

Keywords: corundum megacrysts, immiscible-melt inclusions, underplating basalts, geochemical analysis of inclusions, BSE imaging of corundum

INTRODUCTION

In addition to mantle xenoliths and commonly found megacrysts of augite,

anorthoclase, amphibole and garnet, other megacrysts including corundum, zircon, titanomagnetite and quartz, have been observed in Cenozoic intraplate alkali basalts worldwide. However, the genesis of these megacrysts is highly controversial (e.g., Irving 1986; Guo et al. 1996a,b; Valley et al. 1998; Yui et al. 2003; Saminpanya and Sutherland 2011; Sutherland et al. 2015a,b; Palke et al. 2017; Harris et al. 2017; Baldwin et al. 2017; Baldwin and Ballhaus 2018). The key questions in this debate are: what kind of melts crystallized these megacrysts, and from where were the melts derived?

Major sapphire (or corundum) deposits occur in Tertiary alkali-basalt fields and related alluvial placers (Hughes 1997). They are mainly distributed along the western edge of the Pacific (eastern Australia, Thailand, Cambodia, Laos, Vietnam and eastern China) with some on the west coast of the Indian Ocean (Madagascar, Mozambique and Kenya) and a few in the Atlantic peripheral coast (Sutherland et al. 1998). The genesis of corundum megacrysts is of considerable interest due both for their economic value and for understanding the tectonic setting in which they formed.

There are two main ideas regarding the origin of corundum megacrysts associated with alkali basalts. Some researchers suggest that corundum crystallized directly from alkali basaltic magmas and is thus regarded as a phenocryst in the alkali basalt (Ding 1998; Dong et al. 1999; Han and Xu 2000; Xie et al. 2002). Others indicate that corundum megacrysts were captured by alkali basaltic magmas during their ascent and should be regarded as “xenocrysts”. There are three hypotheses on the origin of corundum xenocrysts: (1) crystallization from different magmas, ranging

93 from phonolitic, syenitic and volatile-rich, or felsic alkaline compositions (Irving
94 1986; Aspen et al. 1990; Coenraads et al. 1990; Oakes et al. 1996; Sutherland 1996;
95 Pakhomova et al. 2006; Monchoux et al. 2006; Pin et al. 2006; Hu et al. 2007); (2)
96 recrystallization due to metamorphism or metasomatism of aluminous rocks
97 (Levinson et al. 1994; Barron et al. 1996; Sutherland et al. 1996); and (3) formation in
98 the mid-lower crust through mixing of carbonate and silicate magmas, or interaction
99 of aluminum-rich rocks with part of the melting products of the metasomatized mantle
100 (Guo et al. 1996a; Yui et al. 2003; Song et al. 2008).

101 Three major occurrences of corundum megacrysts in alkali basalts have been
102 found in eastern China, including Hainan, Mingxi in Fujian Province and Changle in
103 Shandong Province. In this work, we describe unusual melt inclusions in corundum
104 megacrysts from Changle, studied by electron probe microanalysis (EPMA), laser
105 Raman microscopy and Cameca IMS-1280 ion microprobe. The
106 FeO*-SiO_2-Al_2O_3-ZrO_2-rich inclusions found in the Changle corundum megacrysts
107 may provide direct evidence for the origin of the corundum.

108

109 GEOLOGICAL BACKGROUND

110 The Changle region of Shandong Province is the main industrial source of
111 corundum megacrysts (sapphire) in China. These corundum megacrysts are
112 commonly of gem quality and occur primarily in Tertiary alkali basalts and associated
113 alluvial deposits. Basalts erupted episodically in this region, forming the Niushan
114 Formation (18.18±0.79 Ma), the Shanwan Formation (14.11±0.66 Ma) and the

Yaoshan Formation (9.97±0.91 Ma) (Jin 1985, 1989). However, the distribution of the corundum megacryst load amongst the three formations is not clear (Dong et al. 1999; Song et al. 2008). The mining locations of the corundum deposits in basalts are Fangshan, Qiaoguan and Beiyan. The associated alluvial placers are distributed in the Quaternary sediments near Wutu (Fig. 1).

SAMPLE CHARACTERISTICS AND ANALYTICAL METHODS

The studied Changle corundum megacrysts are blue, transparent to semitransparent, and typically 20-30 mm in size (up to ~100 mm). The corundum crystals show distinct oscillatory zoning and abundant primary fluid-melt inclusions under the microscope (Fig. 2 a, b). Narrow black reaction rims (coronas) composed mostly of spinels are developed on the surfaces of the corundum megacrysts (Fig. 2c), at the contact of corundum and the host alkali basalt. At the contact with the megacrysts, basalts have reacted to form a rim of fine-grained titanomagnetite, plagioclase and high-Ti amphibole (Dong et al. 2007; Kong et al. 2017). These disequilibrium reaction rims have been used to argue that the corundum megacrysts are xenocrysts.

To prepare EPMA specimens, the corundum megacrysts were embedded in epoxy resin and polished. The polished mounts were cleaned ultrasonically, dried in air, and finally carbon coated. EPMA and scanning electron microscopy (SEM) measurements were carried out in the State Key Laboratory for Mineral Deposits Research at Nanjing University. For the EPMA analysis, a JEOL JXA-8100 electron

probe microanalyzer was used with an accelerating voltage of 15 keV and a probe current of 20 nA. Because the inclusions are softer than their corundum hosts, they tended to form concave surfaces during polishing. Therefore, for quantitative analyses of the inclusions with the concave surfaces, we used a scanning electron microscope (JEOL JSM-6490) equipped with an X-ray energy dispersive spectrometer (EDS) (Oxford INCAPenta-x3). The working voltage was 20 keV. The peak positions were corrected against Co standards.

Raman spectra were collected using a Renishaw RM2000 laser Raman microscope coupled with an air-cooled CCD detector in the State Key Laboratory for Mineral Deposits Research at Nanjing University. Excitation was achieved using an ionized argon laser tuned to 514 nm. Wave number measurements were done at 23 ℃ and have an accuracy of <2 cm^{-1}. The laser intensity on the surfaces of the samples was 5 mW coupled with a slit width of 50 μm, a grating of 1800 grooves/mm, and a collecting time of 10 s.

U-Pb dating of zircon was conducted using the Cameca IMS-1280 ion microprobe at the Institute of Geology and Geophysics, Chinese Academy of Sciences (IGGCAS) in Beijing and analytical procedures are the same as those described by Li et al. (2009). The O^{2-} primary ion beam was accelerated at 13 kV, with an intensity of *ca* 10 nA. The ellipsoidal spot is about 10×15 μm in size. Positive secondary ions were extracted with a 10 kV potential. Oxygen flooding was used to increase the secondary Pb^{+} sensitivity. In the secondary ion beam optics, a 60 eV energy window was used, together with a mass resolution of *ca* 5400 to separate Pb^{+} peaks from

159 isobaric interferences. A single electron multiplier was used in ion-counting mode to
160 measure secondary ion beam intensities by peak jumping. U-Th-Pb ratios were
161 determined relative to the 337 Ma Plésovice zircon reference material (Sláma et al.
162 2008). Analyses of the standard zircon were interspersed with unknown grains. A
163 long-term uncertainty of 1.5% (1 SD) for $^{206}Pb/^{238}U$ measurements of the standard
164 zircons was propagated to the unknowns (Li et al. 2010), although the measured
165 $^{206}Pb/^{238}U$ error in a specific session is generally around 1% (1 RSD) or less.
166

167 # RESULTS

168 Abundant inclusions in Changle corundum megacrysts have been found during
169 the past decades (e.g. Guo et al. 1996a; Li and Wang 1997; Qiu et al. 1999, 2001; Liu
170 et al. 2007; Song et al. 2008; Liu et al. 2018); the most common are mineral
171 inclusions of oligoclase, zircon, Nb-Ta oxides, carbonate, and fluid-melt inclusions
172 containing a CO_2-rich fluid, daughter minerals and glasses. During the EPMA studies
173 of hundreds of corundum megacrysts recently, we found some unusual inclusions,
174 most of which are mixtures of tiny mineral phases and amorphous substances (AS).
175 The observed mineral phases include corundum, zircon, baddeleyite and quartz (see
176 below for details). The AS are characterized by weak and flat Raman spectra without
177 any peaks. The chemical compositions of the inclusions are dominated by
178 FeO*-SiO_2-Al_2O_3 and ZrO_2.

179 ## Type I inclusions

180 Type I inclusions consist of a glassy phase, bubbles and daughter minerals. They

are usually small (10-30 μm) and dominated by glass (Fig. 2a, b). The identified daughter minerals include augite (Liu et al. 2007) and KCl (Song et al. 2008). Among them, we found solidified, originally melt-dominated inclusions containing tiny crystals of quartz, corundum and baddeleyite (Fig. 2d), ~360 μm across and occurring near the rim of the corundum megacryst. The inclusions consist of a bright part (BP) surrounded by a dark part (DP) in BSE images. The dark part consists mainly of an amorphous substance-1 (AS-1) and 10~30 μm crystals of SiO_2. Raman spectroscopy shows that the SiO_2 crystals are quartz (Fig. 3a), and they make up ~ 20-25 vol % of the dark part. EDS X-ray spectra show that some of the dark part has high Al abundances (Fig. 2f) (together with a small amount of Fe, about 2.1 wt %), which reflect 2~5 vol % of corundum microcrystals (Fig. 2e). In contrast, the bright part consists of AS-2 and ZrO_2 microcrystals up to 5 μm across, which occupy ~30 vol. % of the bright part (Fig. 2g). Raman spectroscopy indicates that the ZrO_2 phase is baddeleyite (Fig. 3b). In addition, a small amount (<1 vol %) of quartz microcrystals occurs in the bright area (Fig. 2h).

To determine the differences in composition between the two parts of the inclusion, we conducted a quantitative compositional analysis using energy dispersive spectrometry (EDS). As shown in Table 1, the baddeleyite (ZrO_2) in the bright part contains small amounts of HfO_2, FeO*, Al_2O_3 and SiO_2; AS-2 consists mainly of FeO* with lower amounts of SiO_2, Al_2O_3 and ZrO_2; AS-1 in the dark part contains less ZrO_2 but more SiO_2. Note that AS-1 is richer in FeO* along the rim of the host corundum than in the center. In addition, small amounts of TiO_2, MnO, MgO, CaO

and K_2O and trace amounts of Na_2O and Cl occur in both AS-1 and AS-2.

Type II inclusions

Type II inclusions are usually smaller, less than 50 μm across. They are composed of zircon, quartz and AS-3. Some of them are dominated by minerals and therefore they are composite inclusions or mineral inclusions. In some cases, small patches (10~30μm) of AS-3 occur independently due to the sectioning effect. These inclusions may have crystallized from an evolved melt, and been captured during the growth of the corundum megacrysts. Fig. 4a shows a micro-dike-like inclusion composed of a zircon "belt" and two areas of AS-3 in a corundum megacryst. Many quartz microcrystals occur along the rim of the zircon belt (Fig. 4b), and a euhedral zircon contains scattered quartz microcrystals (Figs. 4c and 4d). Fig. 4e shows three small irregular patches of FeO*-rich AS-3. EDS analysis indicates that the compositions of AS-3 shown in Figs. 4a and 4e are very similar; they are composed of 70 wt% FeO*, 17 wt% Al_2O_3 and 10 wt% SiO_2 (Table 1). Similar to type I, type II composite inclusions are rich in FeO*-SiO_2-Al_2O_3-ZrO_2. Furthermore, the corundum megacrysts contain abundant acicular inclusions of an Fe oxide; these may be exsolution lamellae, but they are very small (sub-micron) and their mineral assemblage has not been identified. (Fig. 4f).

U-Pb age of the zircon inclusions

It is difficult to find large enough zircons in the corundum megacrysts that are suitable for U-Pb age dating, especially for Type I inclusions. We found several

grains which are either zircon mineral inclusions or Type II inclusions as described above (e.g. grain I-3c in Fig. 5).

The zircons are very young (ca 15 Ma) with very low radiogenic Pb. The common Pb is variably high for the majority of analyses with f_{206} values (the proportion of common ^{206}Pb in total measured ^{206}Pb) between 9.48% and 94.52%. Therefore we list the measured isotopic ratios (common Pb-uncorrected) and the ^{207}Pb-corrected $^{238}U/^{206}Pb$ ages in Table 2. Obviously, one zircon inclusion in a corundum (VII) crystallized at 13-14 Ma. Two zircon inclusions in other two corundums (I-2 and I-3) probably crystallized at 18 Ma (Fig. 5). One analysis for I-2b shows 17.6 Ma; two analyses for I-3c zircon show different ages of 19.0 Ma and 15.3 Ma, but the younger age may be affected by contamination because the analysis spot has partial overlap with the amorphous substance.

DISCUSSION

Are these inclusions of melt?

Abundant fluid-melt inclusions in Changle corundum megacrysts have been found by several research groups (e.g., Li and Wang 1997; Qiu et al. 1999, 2001; Liu et al. 2007; Song et al. 2008). Detailed petrographic observation and laser Raman analyses show that those inclusions are composed of a CO_2 gas component (also containing H_2S and N_2), crystalline Al_2O_3, crystalline Fe-rich opaque phases, and silicate glass along with some unidentified solid phases. In some of the inclusions, Mg-calcite occurs in the walls of cavities (Song et al. 2008).

These multiphase melt inclusions may consist of a glass phase plus one or more

246 bubbles and daughter minerals; they may be ellipsoidal, but more commonly are
247 irregular in shape depending on the crystallized solid phases. The glasses may be
248 either transparent or semi-transparent, and these two kinds of glass may coexist in a
249 single inclusion (Song et al. 2008). These inclusions are commonly from 10 to 30 μm
250 in size, and occur along the growth zones of host corundum megacrysts. The volume
251 percentage of the vapor phase in melt inclusions varies (Liu et al. 2007), and they may
252 be either CO_2-dominated or glass-dominated (more than 90%) (Fig. 2a, b).

253 Among the Type I inclusions we found a novel one with an inferred bubble (in
254 the lower right of Fig. 2d) and two different parts (different amorphous substances),
255 analogous to the above-described micro-textures of the melt inclusions, but large
256 enough to allow an estimation of its composition. The presence of minor zircon,
257 Fe-oxide, oligoclase and quartz mineral inclusions in the corundum megacrysts also
258 implies that they crystallized from a melt rich in Si, Fe, Zr and Al. The coexistence of
259 baddeleyite and quartz in our studied sample is even more interesting. The aggregate,
260 microcrystalline texture is consistent with being a melt inclusion that crystallized after
261 entrapment. The identified minerals and amorphous substances also exclude it from
262 being part of the reaction rim (see the reaction rim assemblage described above and
263 Fig. 2c) of the megacrysts. Another explanation is that the phases represent secondary
264 oxides and clays (or other materials) that adhered to the corundum post emplacement
265 while sitting at the earth's surface. We present observations to exclude this possibility:
266 (1) the volume of the inclusion is completely filled and there is no intergranular space
267 observed in the BSE images of the inclusion; (2) it is mostly composed of glassy

materials without any internal growth textures; (3) the tiny crystals of quartz, corundum and baddeleyite do not crystallize at epithermal or hydrothermal temperatures. We thus interpret it as a melt inclusion of the host corundum megacryst that was either broken or abraded in the magma to expose the inclusion on the surface of the grain. As the Type II inclusions also contain amorphous substances, we consider them along with Type I inclusions for the discussion on initial melt compositions in this paper.

Melt compositions for the inclusions

The composition of melt inclusions are important for understanding the genesis of their host. However, melt inclusions from different localities have a broad range of compositions. Palke et al. (2017) reported glassy melt inclusions with SiO_2 contents between 56.4 wt% and 71.1 wt% in gem-quality sapphires from three alluvial deposits in Montana, USA. The primary melt inclusions represent the silicate liquids that were present at the time of sapphire formation and are enriched in volatile components (8–14 wt%). The melt inclusions in corundums from New England, Australia (Sutherland et al. 1998), show a considerable range in FeO (18-76 wt%), Al_2O_3 (5-31 wt%), SiO_2 (1-34 wt%) and volatile contents (up to 25 wt% by difference).

The estimated melt compositions of the Type I inclusions are listed in Table 3. The bright and dark parts in BSE image account for 15 vol% and 85 vol%, respectively, of the inclusion. In the bright part, baddeleyite and AS-2 account for 30 vol% and 70 vol%, respectively. In the dark part, quartz, corundum and AS-1 account for 22.5 vol%, 3.5 vol% and 74 vol%, respectively.

290 The content of Al_2O_3 accreted to the host corundum in the dark part may be
291 estimated based on the increasing FeO* content towards the rim. Fig. 6 shows inverse
292 linear relationships between the content of FeO* and those of Al_2O_3 and SiO_2.
293 Therefore, the distinct increase in FeO* in AS-1 towards the inclusion rim may be due
294 to crystallization of corundum and quartz phases. However, only a few corundum
295 grains are present in the dark part, and therefore the missing Al_2O_3 has probably
296 accreted to the host corundum megacryst during cooling. The proportion of the
297 missing Al_2O_3 is calculated as:

298 $100 \times (15.82\ wt\% - 6.56\ wt\%)/15.82\ wt\% = 58.53\%$.

299 When the amount of crystallized corundum at the rim of the dark part reached
300 58.53 % of the total Al_2O_3, the content of FeO* in the residual melt would have
301 increased from about 50.81 wt% to 78.66 wt% (Table 1). Fig. 6 shows the variations
302 in FeO* and Al_2O_3 composition and the average compositions of the inner and rim
303 parts of the dark part. The rim accounts for about 15 vol% of the dark part. Thus the
304 amount of the corundum added to the host corundum from the rim of dark part is
305 calculated as follows: $58.53 \times 15\% = 8.78$ vol% of the dark part.

306 The calculated bulk composition of the melt inclusions (Table 3) is rich in FeO*,
307 SiO_2, Al_2O_3 and ZrO_2. The acicular inclusions of Fe-oxide in the corundum also
308 suggest that the corundum megacryst crystallized from a high-FeO* melt. This
309 calculated melt composition is similar to that of melt inclusions in corundums from
310 New England, Australia (Sutherland et al. 1998) (Table 1), but with a higher ZrO_2.
311 Type II inclusions could be derived from more evolved melts, or represent

312 melt-coated mineral inclusions that crystallized from evolved melt, captured because
313 of the growth of corundum megacrysts.

314 A possible analogue to the inclusions described here is found in aggregates of
315 corundum crystals (xenoliths) that occur in the ejecta of Cretaceous pyroclastic
316 basalts in northern Israel (Griffin et al., 2016, 2018; Xiong et al., 2019). The crystals
317 have trapped numerous pockets of Ca-Al-Si oxide melts with percent levels of Ti, Zr
318 and LREE. The melts contain phenocrysts with a wide range of highly-reduced Ti-Zr
319 phases, and then quenched as glass + dmisteinbergite (a polymorph of anorthite)
320 during eruption. Fragments of corundum in the ejecta are commonly coated with, or
321 veined by, a glass that is much richer in Si, Na, K and Ba, and appears to be
322 immiscible with the Ca-Al-Si oxide melts. These glasses crystallize abundant
323 baddeleyite and zircon. While the oxygen-fugacity conditions are clearly different,
324 the Israeli samples suggest a similar underlying mechanism to the one proposed here.

325 In any case, the minerals (zircon and quartz) and AS-3 (Table 1) of the Type II
326 inclusions imply the melt composition was related to that for the Type I inclusions.
327 The melt also contains trace abundances of Na, K, Mn, Ca, Mg and Cl (see Table 1),
328 which are concentrated in daughter minerals such as augite and KCl.

329 We suggest that the dark and bright BSE parts of the Type I inclusions represent
330 two liquid phases formed due to immiscibility of a FeO*-SiO_2-Al_2O_3-ZrO_2-rich melt
331 (see details below): one is relatively rich in ZrO_2 and FeO* but poor in Al_2O_3 and
332 SiO_2 (bright part), and the other is rich in Al_2O_3 and SiO_2 with less FeO* and ZrO_2
333 (dark part). During cooling the melt, which originally occupied the bright area of the

inclusion, crystallized into mainly baddeleyite and minor quartz. Upon further cooling, the remaining melt solidified into the FeO*-rich AS-2. In contrast, the crystallization process of the dark part may be relatively complex, largely due to crystallization of the host corundum. We hypothesize that the Al_2O_3 in the dark part was substantially consumed by incorporation into the host corundum, leading to the relatively high content of FeO* in AS-1 near the host corundum (Table 1, Fig. 6). The increased FeO* content may be ascribed to depletion of Al_2O_3 by the host corundum and subsequent crystallization of quartz from the SiO_2-oversaturated melt. At some point, Al_2O_3 must have become oversaturated and nucleated separately in the AS-1 matrix, resulting in a small amount of matted corundum crystals.

Crystallization of the inclusions

As shown in the phase diagrams of the FeO*-Al_2O_3-SiO_2 and ZrO_2-Al_2O_3-SiO_2 systems (Fig. 7), during crystallization of corundum, the melt on the liquidus surface will be become richer in FeO*-ZrO_2-SiO_2. Liquid immiscibility may occur in both the FeO*-SiO_2 and ZrO_2-SiO_2 systems at T>1600 °C according to experimental studies (Fig. 7), but such temperatures are unlikely here.

The inclusion homogenization temperatures of ~1200 °C obtained by Liu et al. (2007) and Song et al. (2008), are consistent with the homogenization temperatures (1100-1250 °C) of basaltic melt inclusions in general (Danyushevsky et al. 2002), and we suggest that liquid immiscibility probably occurred around these temperatures. The overall liquidus temperatures may have been lowered by the presence of other components (see Table 1), and particularly fluid components, in the melts. However,

356 the ZrO_2-SiO_2 phase diagram (after Butterman and Foster 1967 and Telle et al. 2015,
357 Fig. 8) is instructive as a guide to a possible crystallization path. At some temperature,
358 the melt may separate into two parts, a Zr-rich one corresponding to bright part of the
359 Type I inclusions, and another more Si-rich corresponding to dark part. Then, the
360 Zr-rich part continued to crystallize baddeleyite and possibly zircon, while the Si-rich
361 part continued to crystallize zircon and quartz, both of them accompanied by
362 formation of additional microcrystals of corundum and amorphous substances. The
363 co-existence of baddelyite and quartz in bright BSE images must therefore represent a
364 disequilibrium assemblage.

365 The crystallization history of type II inclusions may be similar to those of Type I
366 inclusions, except that liquid immiscibility did not occur (as reflected by the lack of
367 distinct bright and dark BSE parts of the inclusions). Moreover, as the mineral
368 assemblage is different from Type I inclusions, the Type II inclusions could be derived
369 from more SiO_2-rich melt produced by continued crystallization of its host corundum,
370 consuming some Al_2O_3 from the melt. Another possibility is that the Type II
371 inclusions represent melt-coated mineral inclusions.

372 The role of melt immiscibility in differentiates of basaltic magmas has become
373 widely recognized in recent years, especially since its documentation in the
374 Skaergaard intrusion (Jacobsen et al. 2005). Immiscibility has also been shown to play
375 a major role during several stages of the evolution of the Israeli corundum samples
376 described above, as evidenced by spheres of Fe-Al oxide and Ti-Al oxide melts,
377 spheres of native Fe, and Fe-Ti silicide melts that coexist with the Ca-Al-Si oxide

melts trapped within the corundum. (Griffin et al., 2016, 2018; Xiong et al., 2017). In nearly all cases, one of the conjugate melts is greatly enriched in FeO, and strongly concentrates Zr and other accumulates the divalent and trivalent trace elements (Veksler et al. 2006); these melts may crystallize corundum despite relatively low Al_2O_3 contents, because they are also deficient in SiO_2. We therefore suggest that the inclusion melts reported here represent such immiscible melts.

What was the parental melt of the megacrysts, and where was it generated?

The megacrysts associated with the Tertiary alkali basalt in the Changle region include corundum, zircon, clinopyroxene, titanomagnetite, anorthoclase and quartz. In corundum megacrysts, Fe-oxide exsolution lamellae are commonly seen, with fewer inclusions of zircon, baddeleyite, oligoclase, quartz, Fe-Ti oxide and columbite (this study and Guo et al. 1996a). Guo et al. (1996a) suggested that some inclusions represent an evolved alkaline felsic suite (alkaline granite or syenite, exemplified by feldspar and zircon) and others represent a carbonatitic suite (exemplified by columbite). They also suggested a genetic model: interaction between an alkaline granite or syenite-pegmatite composition (magma or rock) and a carbonatitic magma, at mid-crustal levels, based on the temperature (400 °C) estimated from perthitic feldspar inclusions in Kings Plains corundum. However, a recent study of multiphase melt inclusions (e.g. glass + bubbles + daughter minerals) in Changle corundum megacrysts gave much higher homogenization temperatures of 1040-1300 °C (Liu et al. 2007; Song et al. 2008). In addition, most zircon inclusions in Changle corundum

have $\delta^{18}O$ values from 4.3‰ to 6.1‰, and εHf(t) values from 5.9 to 11.1 (Liu et al. 2018), which are similar with those of coexisting zircon megacrysts (Yu et al. 2010) and strongly suggest a mantle affinity. We therefore suggest it is more likely that the Changle corundum crystallized near the crust-mantle boundary. There is evidence that both alkaline felsic melts and carbonatitic melts existed in the upper mantle beneath Changle. Some spinel lherzolite xenoliths from the nearby Nushan basalts contain amphibole, phlogopite and apatite, as well as thin glass veins. Their compositions imply that the mantle has undergone metasomatism either in sequential events with different compositions (one silicate and one carbonatitic) or by a single event with complex silicate fluids rich in both H_2O and CO_2 components that fractionated and/or evolved during percolation in the lithospheric mantle (Xu et al. 2003). The compositions of glasses show that syenite-type differentiates could be generated (Table 1). These melts may have been derived from metasomatized mantle by the partial melting of deeply subducted materials. The stagnant subducted slab shown in Fig. 1 (Huang and Zhao 2006) illustrates this suggestion.

Regarding the parent melt for the host corundum, it was most likely a syenitic-type differentiate of earlier underplated basalts. The reasons are: (1) $\delta^{18}O$ values of both zircon inclusions (from 4.3‰ to 6.1‰, Liu et al. 2018) and host corundums (from 4.56‰ to 5.65‰, Hu et al. 2007) indicate a mantle affinity; (2) $^{3}He/^{4}He$ and $^{40}Ar/^{36}Ar$ isotopic compositions of noble gases trapped in the corundums from Changle are similar to those of pyroxene, anorthoclase megacrysts, and mantle-derived xenoliths from this region (Hu et al. 2007), and therefore show mantle

source affinity; (3) the corundum megacrysts found in both Niushan Formation basalt (18 Ma) and Yaoshan Formation basalt (*ca* 10 Ma) (Kong et al. 2017 and references there), together with two groups of our new zircon inclusion age data (18 Ma and 13-14 Ma), imply that the basalts are erupted episodically; some large proportion would be underplated (Griffin and O'Reilly 1987), and only rapidly-erupted basalts contain both mantle xenoliths and corundum megacrysts.

IMPLICATIONS

The coexistence of two types of inclusions in the corundum megacrysts sheds new light on magmatic processes that have been proposed, but for which there was little concrete evidence.. The dark and bright parts in BSE image of the type I inclusions record liquid immiscibility at ~1200°C, while the Type II inclusions, composed of zircon, quartz and an amorphous substance, record partly melt component.

When considered together with previously reported mineral inclusions in Changle corundum, the novel inclusions suggest that the corundum megacrysts crystallized from syenitic-type differentiates of basalts, probably underplated at the crust-mantle boundary where slow cooling and melt evolution would be possible. The ages of zircon inclusions show that differentiation predated the eruption of the host basalts by several million years, while the isotopic data suggest that the parental melts were derived from a metasomatized mantle source.

The discovery of these inclusions provides further insights into the genesis of the

corundum megacrysts and the wider megacryst association of corundum-zircon-clinopyroxene-anorthoclase commonly found in intraplate alkali basalts. However, many questions remain to be answered. The development of a full phase diagram for a kind of FeO*-SiO_2-Al_2O_3-ZrO_2-rich melt, at pressures up to at least 1-2 GPa, would place better constraints on the P-T conditions of the proposed differentiation. Application of nano-scale analysis, especially for the amorphous substances, with improved precision and spatial resolution, would be desirable to further reveal the solidification processes of the melt.

ACKNOWLEDGEMENTS

This study was financially supported by the National Natural Science Foundation of China (No. 40730313). Constructive comments and suggestions from the associate editor Callum Hetherington, and careful reviews by Michel Gregoire and two anonymous reviewers are appreciated. Thanks also to Juan Li for assistance in the SEM analysis and Xianhua Li for U-Pb dating. This is contribution xxx from the ARC Centre of Excellence for Core to Crust Fluid Systems (http://www.ccfs.mq.edu.au).

REFERENCES CITED

Aspen, P., Upton, B.G.J., and Dicken, A.P. (1990) Anorthoclase, sanidine and associated megacrysts in Scottish alkali basalts: high pressure syenitic debris from upper mantle sources? European Journal of Mineralogy, 2, 503-517.

Baldwin, L.C., and Ballhaus, C. (2018) Experimental investigation of the reaction between corundum xenocrysts and alkaline basaltic host magma: Constraints on

magma residence times of basalt-hosted sapphires. Lithos, 302, 447-454.

Baldwin, L.C., Tomaschek, F., Ballhaus, C., Gerdes, A., Fonseca, R.O.C., Wirth, R., Geisler, T., and Nagel, T. (2017) Petrogenesis of alkaline basalt-hosted sapphire megacrysts. Petrological and geochemical investigations of in situ sapphire occurrences from the Siebengebirge Volcanic Field, Germany. Contributions to Mineralogy and Petrology, 172, 43.

Barron, L.M., Lishmund, S.R., Oakes, G.M., Barron, B.J., and Sutherland, F.L. (1996) Subduction model for the origin of some diamonds in the Phanerozoic of eastern New South Wales. Australian Journal of Earth Sciences 43, 257-267.

Butterman, W.C., and Foster, W.R. (1967) Zircon stability and the ZrO_2–SiO_2 phase diagram. American Mineralogist. 52, 880–885.

Coenraads, R.R., Sutherland, F.L., and Kinny, P.D. (1990) The origin of sapphires: U-Pb dating of zircon inclusions sheds new light. Mineralogical Magazine 54, 113-122.

Danyushevsky, L.V., McNeill, A.W., and Sobolev, A.V. (2002) Experimental and petrological studies of melt inclusions in phenocrysts from mantle-derived magmas: an overview of techniques, advantages and complications. Chemical Geology 183, 5-24.

Ding, Z.H. (1998) Inclusions in corundum megacryst from alkali basalt, I. The discovery of oligoclase inclusions and its significance. Acta Minerologica Sinica, 18(1): 23-27. (In Chinese with English abstract)

Dong, Z.L., Chen, X.M., Hu, W.X., Wang, R.C., and Zhao, M. (2007) Coronas of

488 corundum megacrysts in the Neogene Changle basalt and its forming model.
489 Acta Petrologica Sinica, 23(4), 805-816. (In Chinese with English abstract)
490 Dong, Z.X., Yang, L.F., and Wang, Y.W. (1999) Study on the origin of the sapphire
491 deposit in the Changle area, Shandong. Acta Geoscientia Sinica, 20(2), 177-183.
492 (In Chinese with English abstract)
493 Griffin, W.L., and O'Reilly, S.Y. (1987) Is the continental Moho the crust-mantle
494 boundary? Geology, 15, 241-244.
495 Griffin, W.L., Gain, S.E.M., Adams, D.T., Huang, J-X., Saunders, M., Toledo, V.,
496 Pearson, N.J. and O'Reilly, S.Y. (2016) First terrestrial occurrence of tistarite
497 (Ti2O3): Ultra-low oxygen fugacity in the upper mantle beneath Mt Carmel, Israel.
498 Geology, 44 (10), 815-818.
499 Griffin, W.L., Huang, J-X., Thomassot, E., Gain, S.E.M., Toledo, V. and O'Reilly, S.Y.
500 (2018) Super-reducing conditions in ancient and modern volcanic systems:
501 Sources and behaviour of carbon-rich fluids in the lithospheric mantle.
502 Mineralogy and Petrology, 112 (Suppl 1):S101–S114.
503 Guo, J.F., O'Reilly, S.Y., and Griffin, W.L. (1996a) Corundum from basaltic terrains: a
504 mineral inclusion approach to the enigma. Contributions to Mineralogy and
505 Petrology, 122, 368-386.
506 Guo, J.F., O'Reilly, S.Y., and Griffin, W.L. (1996b) Zircon inclusions in corundum
507 megacrysts: I. Trace element geochemistry and clues to the origin of corundum
508 megacrysts in alkali basalts. Geochemica et Cosmochimica Acta, 60, 2347-2363.
509 Han, M., and Xu, Y.T. (2000) Study of the primary oribodies of sapphire in Shandong

province. Journal of Shandong Normal University (Natural Science), 15, 288-293. (In Chinese with English abstract)

Harris, S.J., Graham, I.T., Lay, A., Powell, W., Belousova, E., and Zappettini, E. (2017) Trace element geochemistry and metasomatic origin of alluvial sapphires from the Orosmayo region, Jujuy Province, Northwest Argentina. The Canadian Mineralogist 55(4), 595-617.

Hu, W.X., Song, Y.C., Chen, X.M., Tao, M.X., and Zhang, L.P. (2007) Noble gases in corundum megacrysts from the basalts in Changle, Shandong Province, eastern China. Chinese Science Bulletin, 52, 380-387.

Huang, J.L., and Zhao, D.P. (2006) High-resolution mantle tomography of China and surrounding regions. Journal of Geophisical Research, 111: B09305, doi:10.1029/2005JB004066.

Hughes, R.W. (1997) Ruby and sapphire. RWH Publishing, Boulder, Co, USA, 512pp.

Irving, A.J. (1986) Polybaric magma mixing in alkali basalts and kimberlites: evidence from corundum, zircon and ilmenite megacrysts. 4th Int Kimberlite Conf Perth Geol Soc Aust Abstr Ser 16: 262-264.

Jakobsen, J.K., Veksler, I.V., Tegner, C., and Brooks, C.K. (2005) Immiscible iron- and silica-rich melts in basalt petrogenesis documented in the Skaergaard intrusion. Geology, 33, 885–888

Jin, L.Y. (1985) K-Ar ages of Cenozoic volcanic rocks in the middle segment of the Tancheng-Lujiang Fault zone and stages of related volcanic activity. Geological

532 Review, 31(4), 309-315. (In Chinese with English abstract)

533 Jin, L.Y. (1989) Petrologic and geochemical characteristics of Cenozoic volcanic
534 rocks in the middle segment of the Tancheng-Lujiang fault zone. Acta
535 Petrologica Sinica, 4, 45-57. (In Chinese with English abstract)

536 Kong, F.M., Li, X.P., Zhao, L.Q., Chen, S., and Yin, Q.H. (2017) Petrography and
537 Mineral Chemistry of Corundum and Spinel Menocryst in the Cenozoic Basalt at
538 Changle, Shandong Prinvice. Geological Review, 63(2), 441-457. (In Chinese
539 with English abstract)

540 Levin, E.M., Robbins, C.R., and McMurdie, H.F. (1974) In Phase Diagrams for
541 Ceramists, ed. M. K. Reser. The American Ceramic Society, Columbus, OH,
542 Figs 772.

543 Levinson, A.A., and Cook, F.A. (1994) Gem corundum in alkali basalt: origin and
544 occurrence. Gems Gemol 30: 253-262.

545 Li, G.C., and Wang, P., (1997) Morphological characters of the natural inclusions and
546 their distribution in the Shandong corundum and sapphire. Mineral Resources
547 and Geology, 11(2): 104-108. (In Chinese with English abstract)

548 Li, Q.L., Li, X.H., Liu, Y., Tang, G.Q., Yang, J.H., and Zhu, W.G. (2010) Precise U-Pb
549 and Pb-Pb dating of Phanerozoic baddeleyite by SIMS with oxygen flooding
550 technique. Journal of Analytical Atomic Spectrometry, 25, 1107–1113.

551 Li, X.H., Liu, Y., Li, Q.L., Guo, C.H., and Chamberlain, K.R. (2009) Precise
552 determination of Phanerozoic zircon Pb/Pb age by multi-collector SIMS without
553 external standardization. Geochemistry Geophysics Geosystem 10, Q04010.

554 doi:10.1029/cGC002400.

555 Liu, J.Q., Ni, P., Shen, K., and Ding, J.Y. (2007) Liquid immiscibility recorded in melt
556 inclusions within corundum from alkaline basalt, Changle area, Shangdong
557 province, Eastern China. Acta Petrologica Sinica, 23(1): 125-130.

558 Liu, Z.H., Su, F., Yang, S.H., Liu, Y., and He, H.Y. (2018) Geochemical characteristics
559 of zircon inclusions from Changle corundum in Shandong Province. Geochimica
560 47(1):48-62. (In Chinese with English abstract)

561 Monchoux, P., Fontan, F., De, and Parseval, P. (2006) Igneous albitite dikes in
562 orogenic lherzolites, western Pyrenees, France: A possible source for corundum
563 and alkali feldspar xenocrysts in basaltic terranes. I. Mineralogical associations.
564 The Canadian Mineralogist, 44, 817-842.

565 Oakes, G.M., Barron, L.M., and Lishmund, S.R. (1996) Alkali basalts and associated
566 volcaniclastic rocks as a source of sapphire in Eastern Australia. Australian
567 Journal of Earth Sciences, 43, 289-298.

568 Pakhomova, V.A., Zalishchak, B.L., Odarichenko, E.G., Lapina, M.I., and Karmanov.
569 N.S. (2006) Study of melt inclusions in the Nezametnoye corundum deposit,
570 Primorsky region of the Russian Far East: Petrogenetic consequences. Journal of
571 Geochemical Exploration, 89, 302-305.

572 Palke, A.C., Renfro, N.D., and Berg, R.B. (2017) Melt inclusions in alluvial sapphires
573 from Montana, USA: Formation of sapphires as a restitic component of lower
574 crustal melting? Lithos, 278-281, 43-53.

575 Pin, C., Monchoux, P., and Paquette, J.L. (2006) Igneous albitite dikes in orogenic

lherzolites, western Pyrenees, France: A possible source for corundum and alkali feldspar xenocrysts in basaltic terranes. II. Geochemical and petrogenetic considerations. The Canadian Mineralogist, 44, 843-856.

Qiu, Z. L., Chen, B. H., and Chen, J. D. (1999) Discovery of zircon inclusions in corundum megacrysts related to alkali basalt in Changle, Shandong. Acta Scientiarum Naturalium, Universitatis Sunyatseni, 38(6): 131 -132. (In Chinese with English abstract)

Qiu, Z. L., Chen, J. D., Chen, B. H., and Zhu, M. (2001) The forming of corundum megacrysts related to alkali basalt in Changle, Shandong. Acta Scientiarum Naturalium, Universitatis Sunyatseni, 40(2): 107 -111. (In Chinese with English abstract)

Saminpanya, S., and Sutherland, F.L. (2011) Different origins of Thai area sapphire and ruby, derived from mineral inclusions and co-existing minerals. European Journal of Mineralogy, 23(4), 683-694.

Sláma, J., Košler, J., Condon, D.J., Crowley, J.L., Gerdes, A., Hanchar, J.M., Horstwood, M.S.A., Morris, G.A., Nasdala, L., Norberg, N., Schaltegger, U., Schoene, B., Tubrett, M.N., and Whitehouse, M.J. (2008) Plešovice zircon—A new natural reference material for U-Pb and Hf isotopic microanalysis. Chemical Geology, 249, 1–35.

Song, Y.C., Wu, W.X., and Zhang, W.L. (2008) Micro-thermometry and Raman density analysis of fluid and melt inclusions in corundum megacrysts from basalts in Changle, Shandong Province. Acta Petrologica et Mineralogica 27 (6),

489-504. (In Chinese with English abstract)

Sutherland, F.L. (1996) Alkaline rocks and gemstones, Australia: a review and synthesis. In: Sutherland FL (ed) The Nicholas Rock symposium: alkaline rocks and their associated mineralization. Australian Journal of Earth Sciences, 43, 323-343.

Sutherland, F.L., Hoskin, P.W.O., and Fanning. C.M. (1998) Models of corundum origin from alkali basaltic terrains: a reappraisal. Contributions to Mineralogy and Petrology, 133(4), 356-372.

Sutherland, F.L., Piilonen, P.C., Zaw, K., Meffre, S., and Thompson, J. (2015a) Sapphire within zircon-rich gem deposits, Bo Loei, Ratanakiri Province, Cambodia: trace elements, inclusions, U-Pb dating and genesis. Australian Journal of Earth Sciences, 62(6), 761-773.

Sutherland, F.L., Coenraads, R.R., Abduriyim, A., Meffre, S., Hoskin, P.W.O., Giuliani, G., Beattie, R., Wuhrer, R., and Sutherland, G.B. (2015b) Corundum (sapphire) and zircon relationships, Lava Plains gem fields, NE Australia: Integrated mineralogy, geochemistry, age determination, genesis and geographical typing. Mineralogical Magazine, 79(3), 545-581.

Telle, R., Greffrath, F., and Prieler, R. (2015) Direct observation of the liquid miscibility gap in the zirconia–silica system. Journal of the European Ceramic Society, 35, 3995–4004.

Valley, J.W., Kinny, P.D., Schulze, D.J., and Spicuzza, M.J. (1998) Zircon megacrysts from kimberlite: oxygen isotope variability among mantle melts.

620 Contributions to Mineralogy and Petrology, 133, 1-11.

621 Veksler, V., Dorfman, A.M., Danyushevsky, L.V., Jakobsen, J.K., and Dingwell, D.
622 (2006) Immiscible silicate liquid partition coefficients: implications for
623 crystal-melt element partitioning and basalt petrogenesis. Contributions to
624 Mineralogy and Petrology, 152, 685-702.

625 Xie, H.S., Zhu, W.G., and Hou, W. (2002) Discovery of corundum in alkali basalt at
626 high temperature and high pressure. Journal of Physics-Condensed Matter,
627 14(44), 11365-11368.

628 Xiong, Q., Griffin, W.L., Huang, J-X., Gain, S.E.M., Toledo, V., Pearson, N.J. and
629 O'Reilly, S.Y. (2017) Super-reduced mineral assemblages in "ophiolitic"
630 chromitites and peridotites: The view from Mt Carmel. European Journal of
631 Mineralogy, 29, 557-570.

632 Xu, X.S., O'Reilly, S.Y., Griffin, W.L., and Zhou, X.M. (2003) Enrichment of upper
633 mantle peridotite: petrological, trace-element and isotopic evidence in xenoliths
634 from SE China. Chemical Geology, 198 (3-4), 163-188.

635 Yu, Y., Xu, X.S., and Chen, X.M. (2010) Genesis of zircon megacrysts in Cenozoic
636 alkali basalts and the heterogeneity of subcontinental lithospheric mantle, eastern
637 China. Mineralogy and Petrology, 100: 75-94.

638 Yui, T.F., Khin, Zaw., and Limtrakun, P. (2003) Oxygen isotope composition of the
639 Denchai sapphire, Thailand: a clue to its enigmatic origin. Lithos, 67, 153–161.

640 Zhu, G., Song, C.Z., Niu, M.L., Liu, G.S., and Wang, Y.S. (2002) Lithospheric
641 textures of the Tan-Lu Fault Zone and their genetic analysis. Geological Journal

642 of China Universities, 8, 256-264.

643

644 **FIGURE CAPTIONS**

645 **FIGURE 1**. Sketch geological map of the Fangshan area in Changle, Shandong
646 Province, eastern China. 1, Quaternary alluvium, proluvium and eluvium
647 sediments; 2, Tertiary alkali basalts; 3, middle-late Tertiary Wutu formation
648 (shale); 4, Cretaceous Wangshi formation (sandstone and sandy shale); 5,
649 Archaean granitic gneiss; 6, placer corundum deposits (modified after Dong et al.
650 1999 and Zhu et al. 2002). The dotted curve in the uppper-left inset represents
651 the western edge of the stagnant slab in the mantle transition zone (Huang and
652 Zhao 2006).

653 **FIGURE 2**. Characteristics of type I inclusions in a corundum (Crn) megacryst from
654 Changle, Shangdong Province, eastern China. a and b, Fluid-melt inclusions
655 fully enclosed in corundum megacrysts, Gl–glass, Bb–bubble, Dm–daughter
656 mineral (Liu et al. 2007); c, Reaction rim on corundum megacryst, Spl–spinel,
657 Mag–magnetite, Pl–plagioclase; d, Backscattered electron (BSE) image of the
658 Type I inclusion; e, BSE image of the corundum (Crn) microcrystal in
659 amorphous substance-1 (AS-1, an enlarged view of the small white box in Fig.
660 2d); f, Al element map in the same area as Fig. 2e; g, Baddeleyite (Bdy)
661 microcrystals distributed in amorphous substance-2 (AS-2, an enlarged view of
662 the black box in Fig. 2d); h, A quartz (Qz) microcrystal in BP.

663 **FIGURE 3**. Raman spectra showing crystals of quartz and baddeleyite (three grains

each) in a Type I inclusion.

FIGURE 4. Characteristics of the Type II inclusions. a, BSE image of a microdike-like inclusion composed of a zircon (Zrn) "belt" and amorphous substance-3 (AS-3) in a corundum (Crn) megacryst; b, Quartz (Qz) microcrystals occur along the rim of the zircon (an enlarged view of the white box in Fig. 4a); c, BSE image of a euhedral zircon. Note that some quartz microcrystals occur in the interior of the zircon or surrounding it; d, X-ray scanning image of Si element for the same area as Fig. 4c; e, BSE image of the FeO*-rich amorphous substance-3 (AS-3); f, BSE image of the acicular Fe oxide.

FIGURE 5. U-Pb dating of zircon inclusions (Type II inclusions) using the Cameca IMS-1280 ion microprobe.

FIGURE 6. Variations of FeO* content with Al_2O_3 and SiO_2 contents in the amorphous substance-1 in the DP.

FIGURE 7. FeO*-Al_2O_3-SiO_2 (a) and ZrO_2-Al_2O_3-SiO_2 (b) phase diagrams (modified from http://www.crct.polymtl.ca/fact/download.php, PhaseDiagrams, DemoFigs, FToxid Figs, and Levin et al. 1974).

FIGURE 8. Binary ZrO_2-SiO_2 phase diagram (modified from Butterman and Foster (1967) and Telle et al. (2015)), illustrating the temperatures of the two-liquid phase region. Numbers 7-8 and 9-10 are metastable immiscibility pairs with one ZrO_2-rich and another SiO_2-rich, respectively. Dark part (DP) and bright part (BP) are the immiscibility pair of the studied Type I inclusion.

This is the peer-reviewed, final accepted version for American Mineralogist, published by the Mineralogical Society of America.
The published version is subject to change. Cite as Authors (Year) Title. American Mineralogist, in press.
DOI: https://doi.org/10.2138/am-2020-7347. http://www.minsocam.org/

TABLE 1. Compositions of the Type I and Type II inclusions in corundum megacrysts analyzed by EDS (wt%).

	n	SiO_2	Al_2O_3	FeO*	ZrO_2	HfO_2	TiO_2	MnO	MgO	CaO	Na_2O	K_2O	Cl
Type I:													
Baddeleyite	16	0.08~1.57[a]	0.52~3.70	1.84~8.45	84.04~93.53	3.44~4.93							
		0.83[b]	1.94	4.57	89.21	4.08							
AS-2	69	0.73~23.35	0.73~15.17	50.59~90.24	2.21~29.46								
		11.23	8.37	69.77	8.34	0.15	0.24	0.58	0.35	0.68	0.47	0.58	0.16
AS-1	74	22.97	13.44	57.96	0.16	-	0.75	1.34	0.98	0.71	0.15	1.43	0.11
AS-1(rim)	19	3.16~14.38	2.41~10.25	71.59~87.97									
		9.94	6.56	78.66	0.16	-	0.36	1.88	0.05	0.64	0	1.18	0.04
AS-1(inner)	55	16.33~42.00	9.58~24.42	26.98~68.03									
		27.32	15.82	50.81	0.16	-	0.85	1.21	1.22	0.73	0.19	1.49	0.12
Quartz	5	94.31~97.15	0.54~2.72	2.23~3.25									
		95.68	1.39	2.76									
Type II:													
Zircon	5	31.35~34.84	0.42~1.53	0.12~0.81	61.97~64.89	1.70~3.16							
		32.43	1.04	0.26	63.68	2.59							
AS-3	31	2.43~23.30	5.90~38.78	45.82~88.27									
		9.90	17.38	70.34	-	-	0.86	-	0.50	0.27	-	0.13	0.1[c]
Quartz	4	97.42	2.14	0.44									
Melt inclusions in corundum megacrysts from New England, Australia (Sutherland et al. 1998):													
		1~34	5~31	18~76									
Silicate glass		22.16	20.39	43.54			0.47		0.05	0.07		0.04	
Fe-rich glass		3.88	9.96	68.55			0.59		0.07	0.23		0.00	
Melt compositions of glass in mantle xenolith from Nushan, China (Xu et al. 2003):													
		43.1	31.58	6.11			1.66	0.03	2.00	3.86	0.35	0.30	
		51.5	20.56	6.40			1.59	0.07	0.75	4.11	5.53	2.53	

Notes: n is the number of analysis. FeO* is the total of FeO and Fe_2O_3. [a] variation range; [b] average; [c] includes Cr_2O_3 0.51 wt%. AS-amorphous substance

This is the peer-reviewed, final accepted version for American Mineralogist, published by the Mineralogical Society of America.
The published version is subject to change. Cite as Authors (Year) Title. American Mineralogist, in press.
DOI: https://doi.org/10.2138/am-2020-7347. http://www.minsocam.org/

TABLE 2. U–Pb isotopic data for zircon inclusions (Type II inclusions)

Sample/ spot no.	U (ppm)	Th (ppm)	Th/U	$^{206}Pb/^{204}Pb$ measured	f_{206}%	$^{238}U/^{206}Pb$	± 1s (%)	$^{207}Pb/^{206}Pb$	± 1s (%)	207-corr age (Ma)	± 1s (Ma)
VII-1a@1	979	622	0.635	197	9.48	436.460	3.39	0.08133	6.73	14.1	0.5
VII-1a@2	244	117	0.482	20	94.52	78.049	6.51	0.72253	2.29	11.3	9.3
VII-1a@3	193	70	0.364	22	84.14	159.828	9.09	0.58015	4.13	12.8	3.9
VII-1a@4	406	105	0.258	37	50.16	287.481	3.45	0.35243	5.11	13.7	1.3
VII-1a@5	214	157	0.733	33	57.38	286.740	6.56	0.38967	5.51	12.6	1.6
VII-1a@6	183	123	0.671	24	78.75	245.766	12.85	0.44467	11.37	12.9	2.9
I-2b@2	287	135	0.472	35	54.05	204.161	2.70	0.39231	4.75	17.6	2.0
I-3c@1	2431	2701	1.111	51	36.46	206.276	5.12	0.35392	6.94	19.0	2.1
I-3c@2	3589	4863	1.355	143	13.11	378.108	2.73	0.12379	17.05	15.3	0.7

Note: $^{238}U/^{206}Pb$ and $^{207}Pb/^{206}Pb$ values are not corrected for common lead. f_{206}% is the fraction of ^{206}Pb that is common Pb in percent.

TABLE 3. Calculated bulk composition of the melt in the inclusions (wt%)

	Volume (%)	SiO_2	Al_2O_3	FeO*	ZrO_2	Total
BP	15%	8.11	6.44	50.21	32.60	97.36
DP*		38.53	13.76	43.51	0.12	95.91
DP	85%	35.14	21.33	39.69	0.11	96.27
Melt		31.08	19.10	41.27	4.98	96.43

Notes: BP=(Baddeleyite×30+(AS-2) ×70)/100 ; DP*=(Quartz×22.5+(AS-1) ×74+Corundum×3.5)/100;
DP=(DP*×91.22+ Corundum×8.78)/100; Melt=(BP×15+ DP×85)/100

723
724
725

726 **FIGURES:**

727

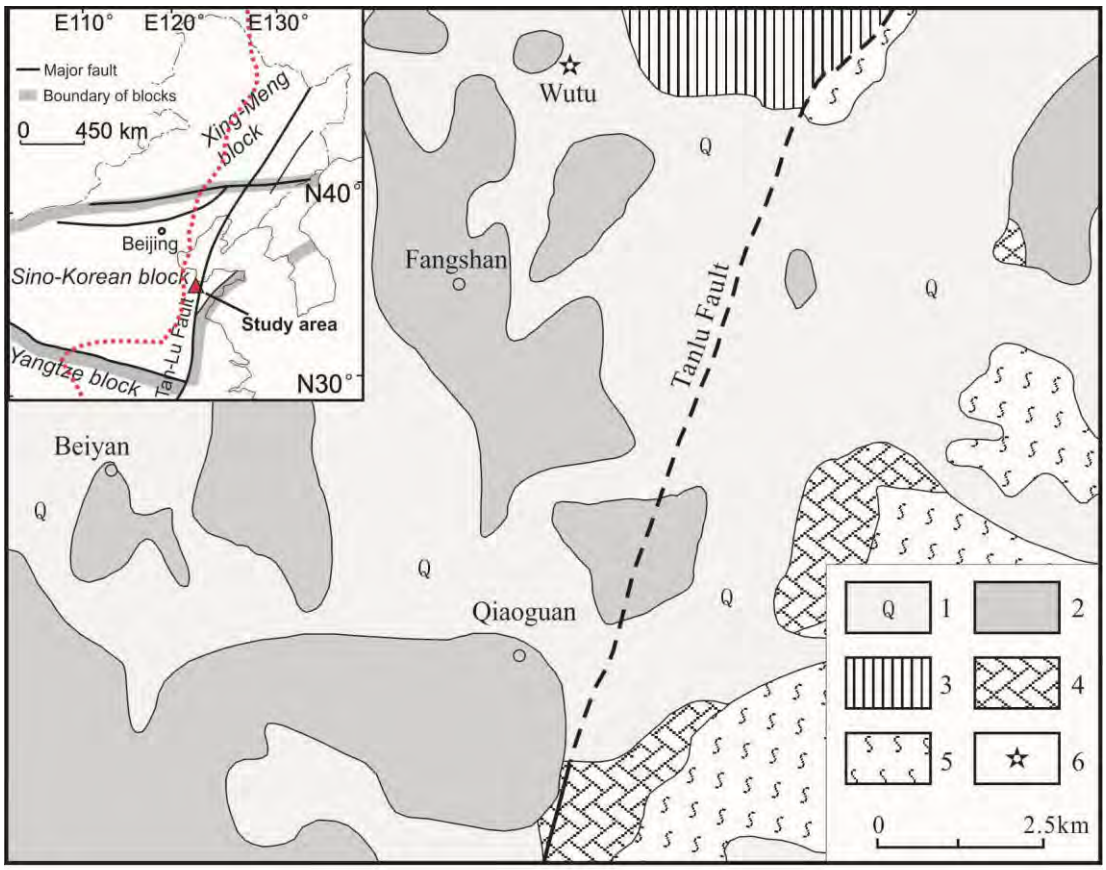

Fig. 1

728
729

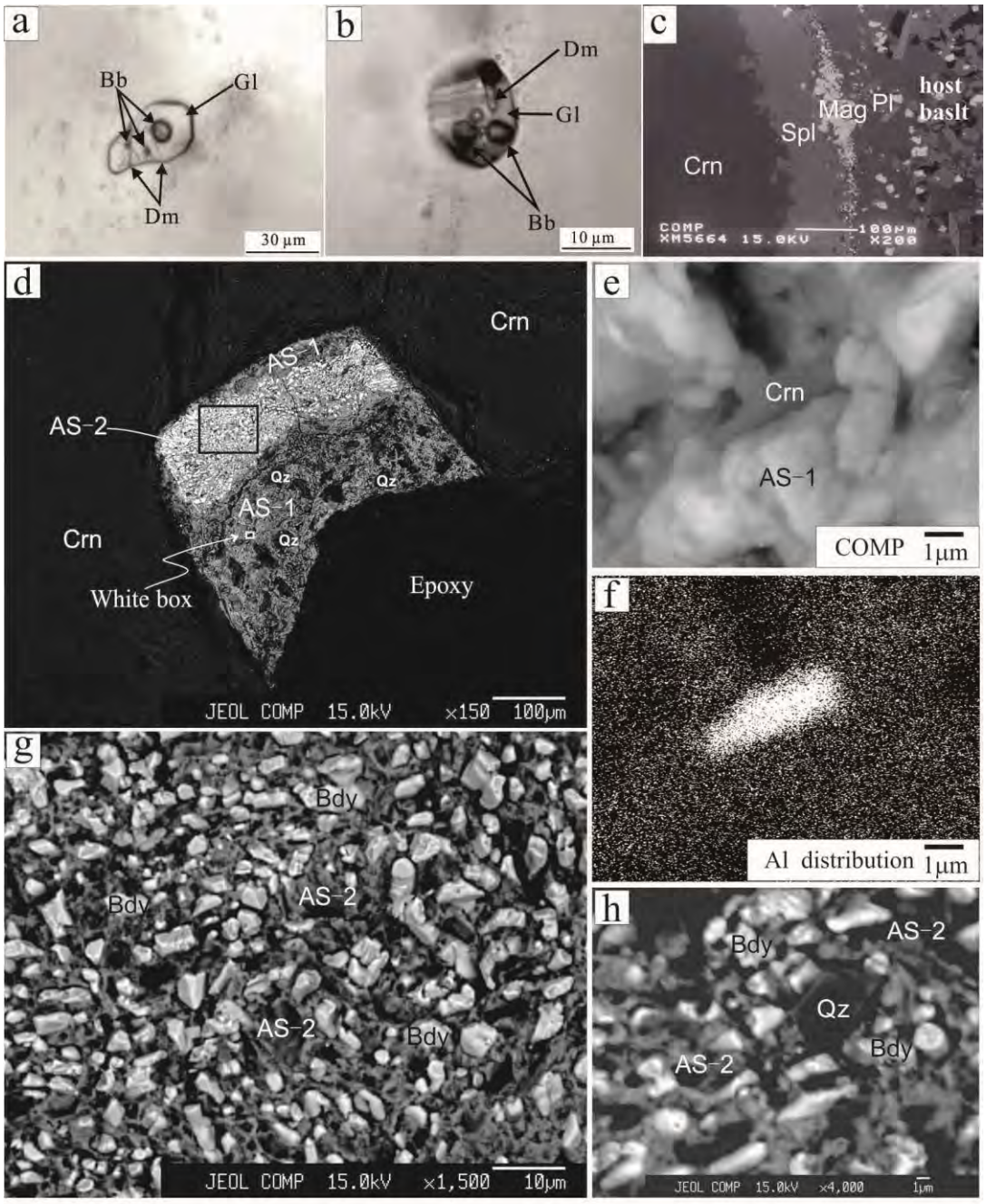

Fig. 2

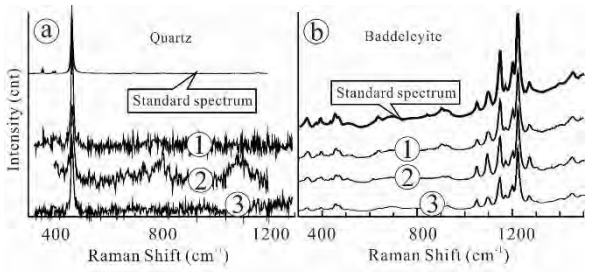

Fig. 3

738
739

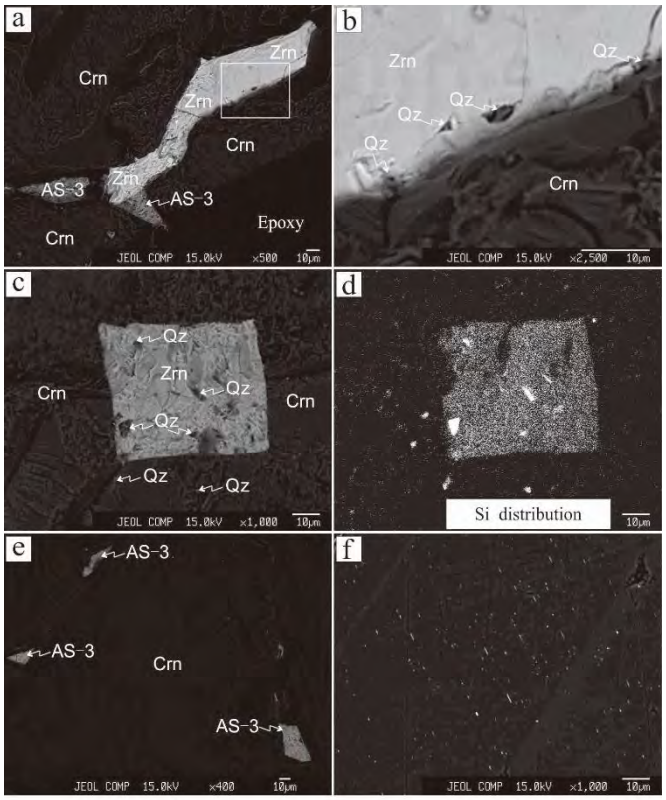

Fig. 4

740
741

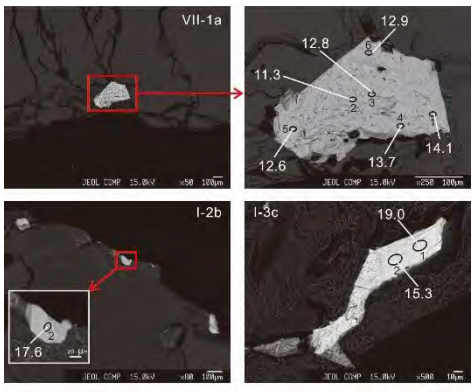

Fig. 5

742
743
744

This is the peer-reviewed, final accepted version for American Mineralogist, published by the Mineralogical Society of America.
The published version is subject to change. Cite as Authors (Year) Title. American Mineralogist, in press.
DOI: https://doi.org/10.2138/am-2020-7347. http://www.minsocam.org/

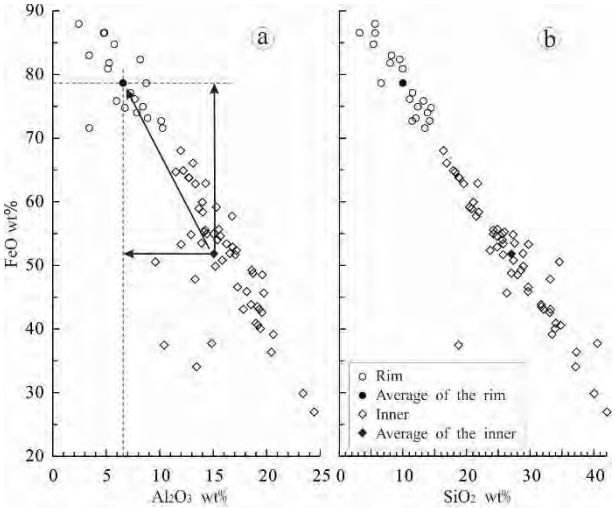

Fig. 6

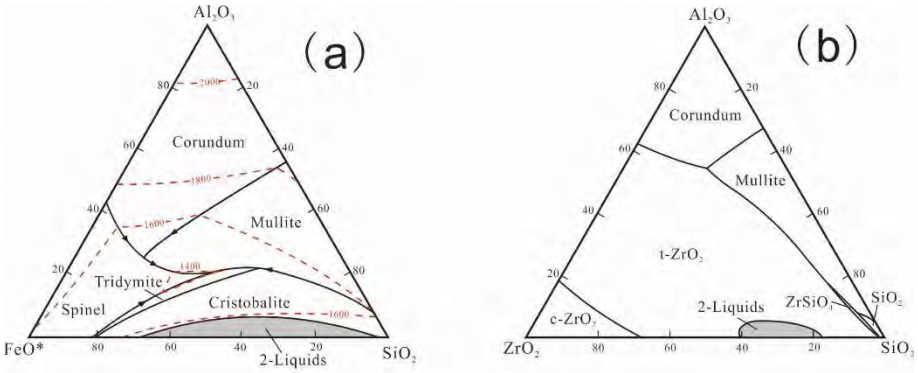

Fig. 7

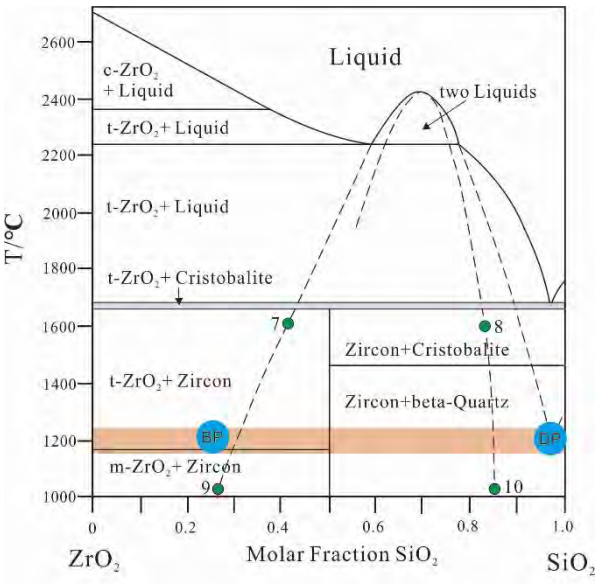

Fig. 8

This is the peer-reviewed, final accepted version for American Mineralogist, published by the Mineralogical Society of America.
The published version is subject to change. Cite as Authors (Year) Title. American Mineralogist, in press.
DOI: https://doi.org/10.2138/am-2020-7347. http://www.minsocam.org/

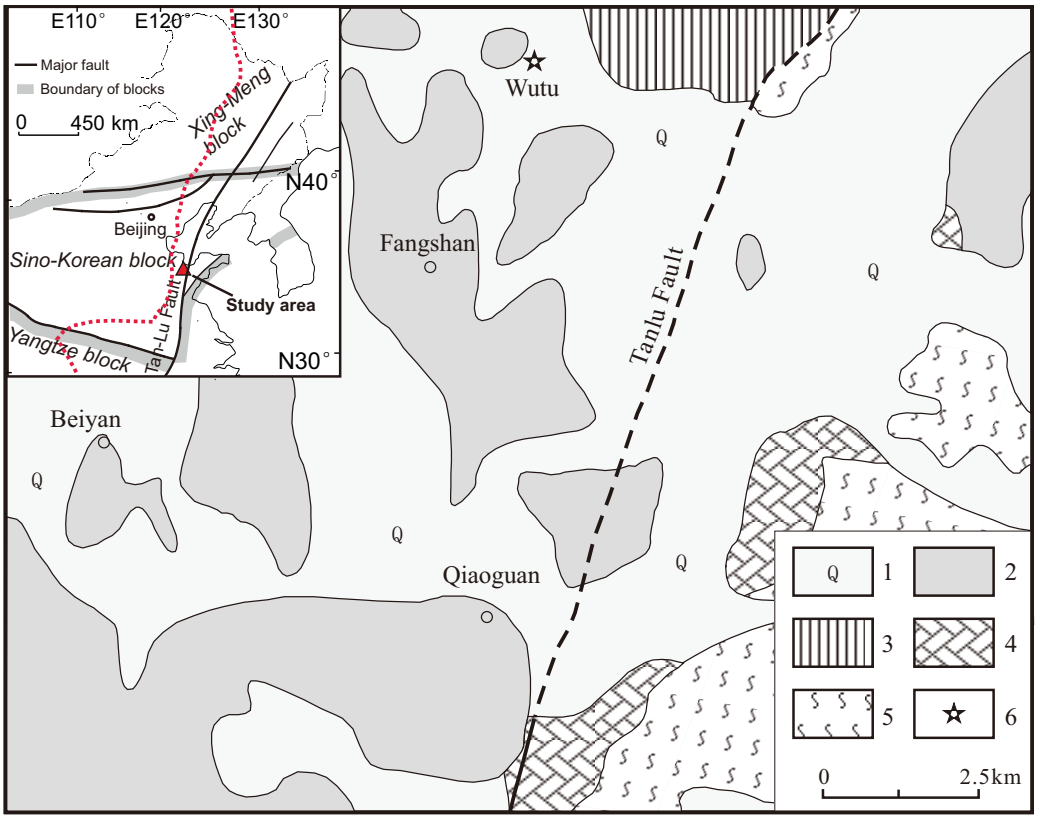

Fig. 1

This is the peer-reviewed, final accepted version for American Mineralogist, published by the Mineralogical Society of America.
The published version is subject to change. Cite as Authors (Year) Title. American Mineralogist, in press.
DOI: https://doi.org/10.2138/am-2020-7347. http://www.minsocam.org/

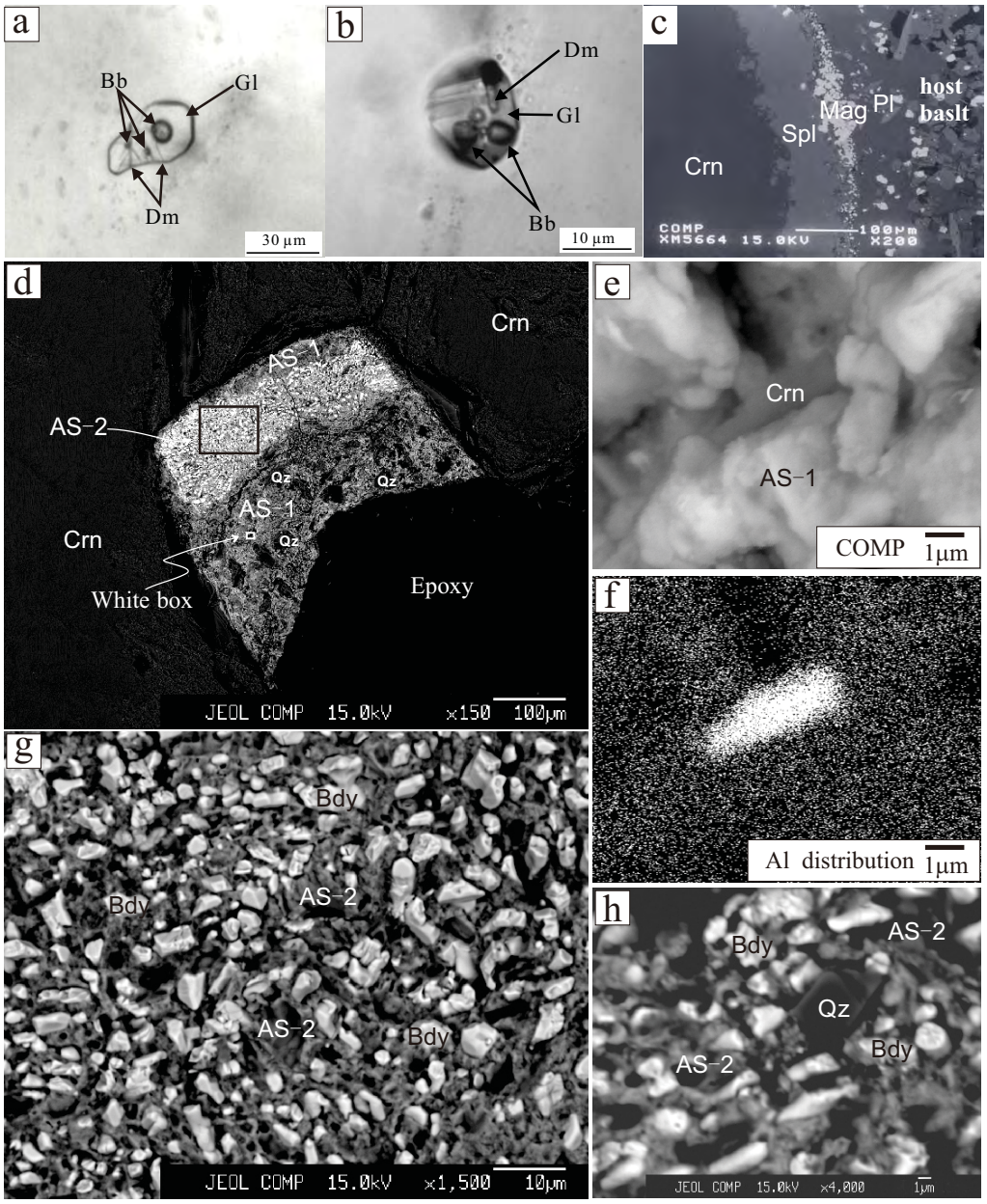

Fig. 2

This is the peer-reviewed, final accepted version for American Mineralogist, published by the Mineralogical Society of America.
The published version is subject to change. Cite as Authors (Year) Title. American Mineralogist, in press.
DOI: https://doi.org/10.2138/am-2020-7347. http://www.minsocam.org/

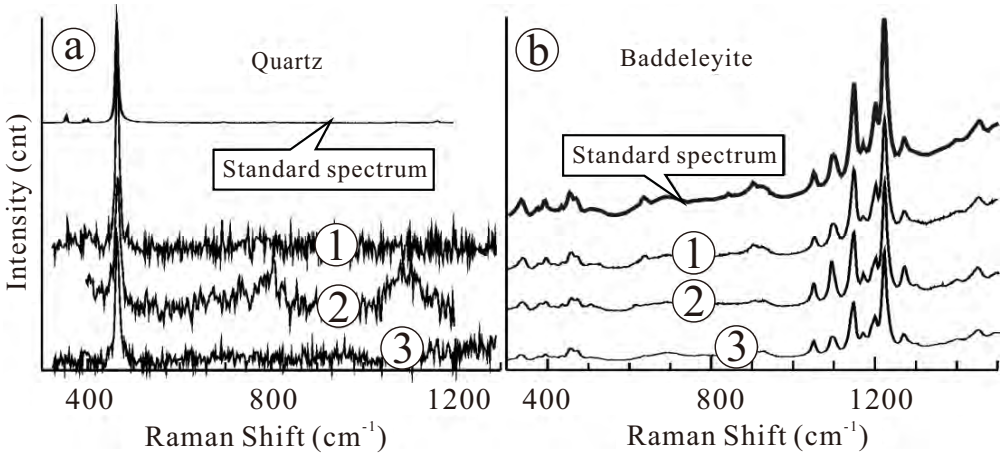

Fig. 3

This is the peer-reviewed, final accepted version for American Mineralogist, published by the Mineralogical Society of America.
The published version is subject to change. Cite as Authors (Year) Title. American Mineralogist, in press.
DOI: https://doi.org/10.2138/am-2020-7347. http://www.minsocam.org/

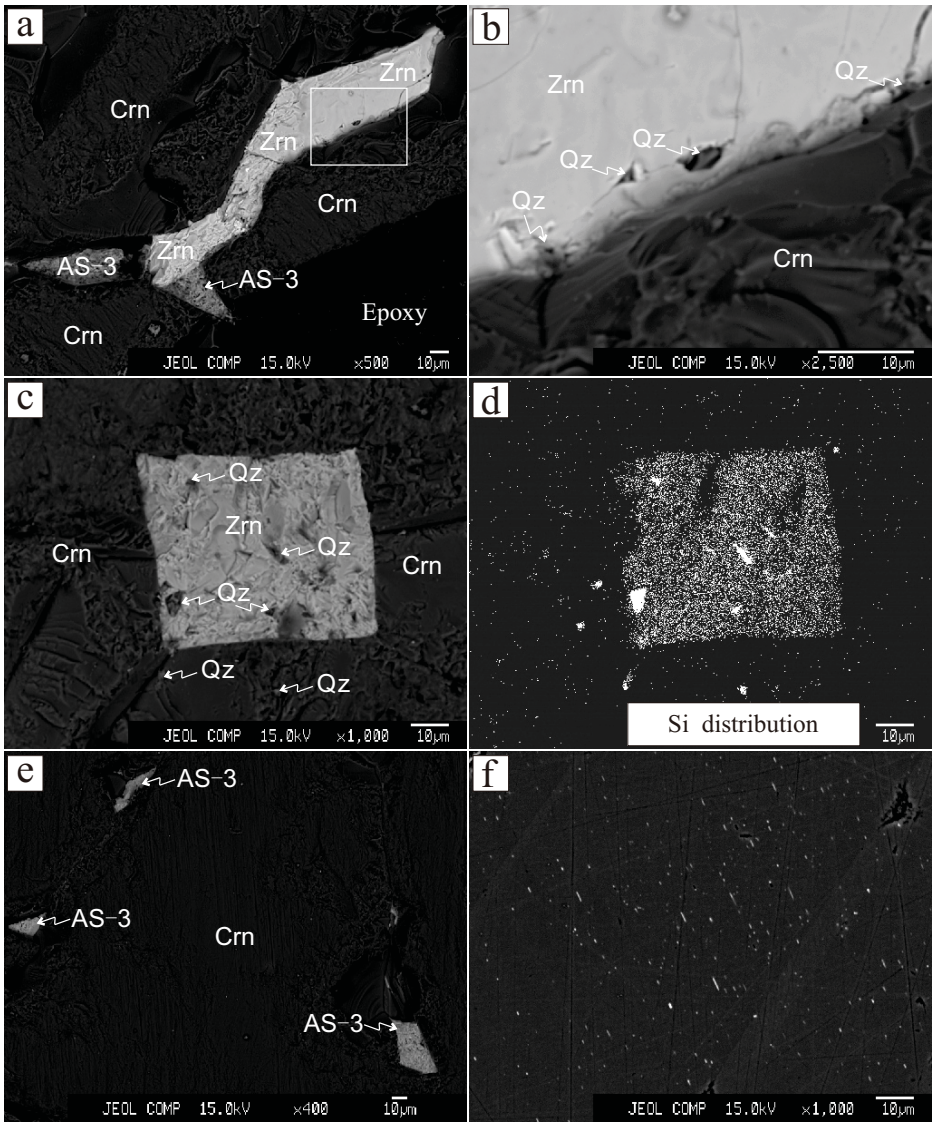

Fig. 4

This is the peer-reviewed, final accepted version for American Mineralogist, published by the Mineralogical Society of America.
The published version is subject to change. Cite as Authors (Year) Title. American Mineralogist, in press.
DOI: https://doi.org/10.2138/am-2020-7347. http://www.minsocam.org/

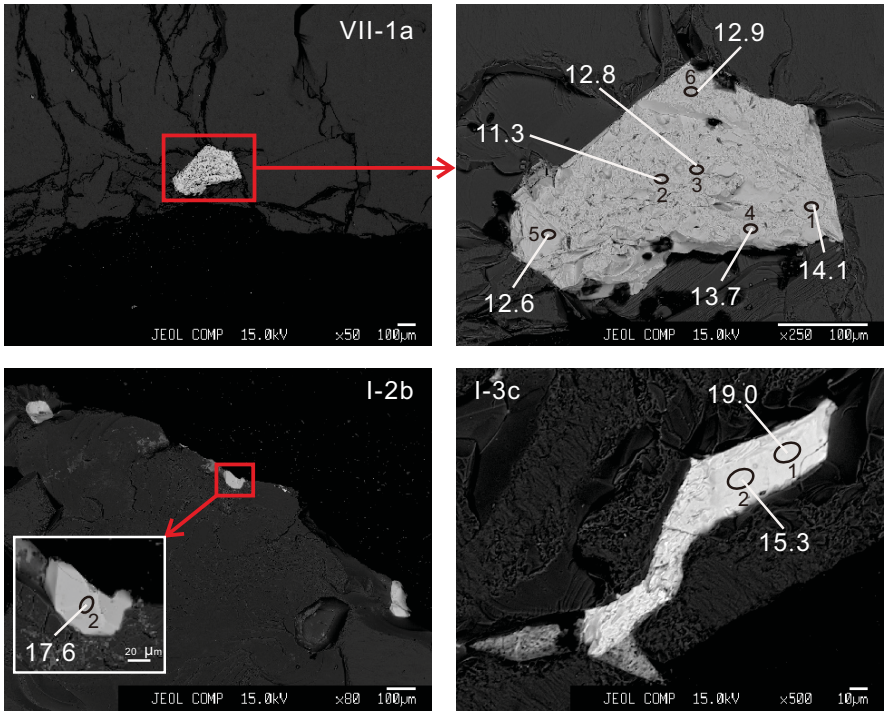

Fig. 5

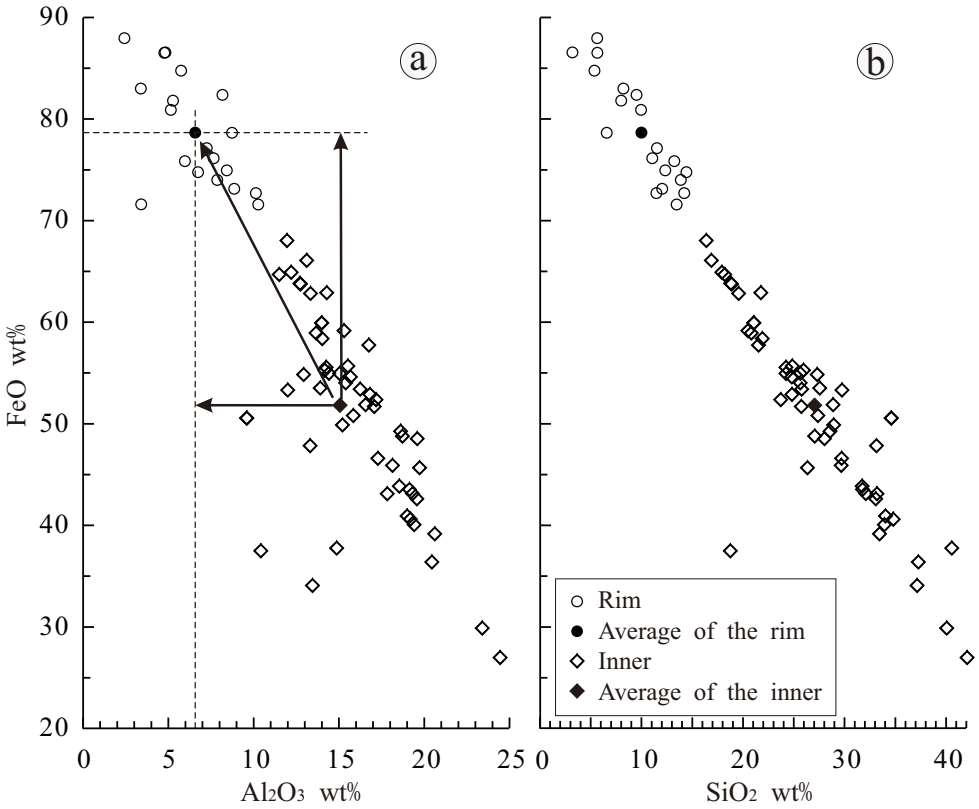

Fig. 6

This is the peer-reviewed, final accepted version for American Mineralogist, published by the Mineralogical Society of America.
The published version is subject to change. Cite as Authors (Year) Title. American Mineralogist, in press.
DOI: https://doi.org/10.2138/am-2020-7347. http://www.minsocam.org/

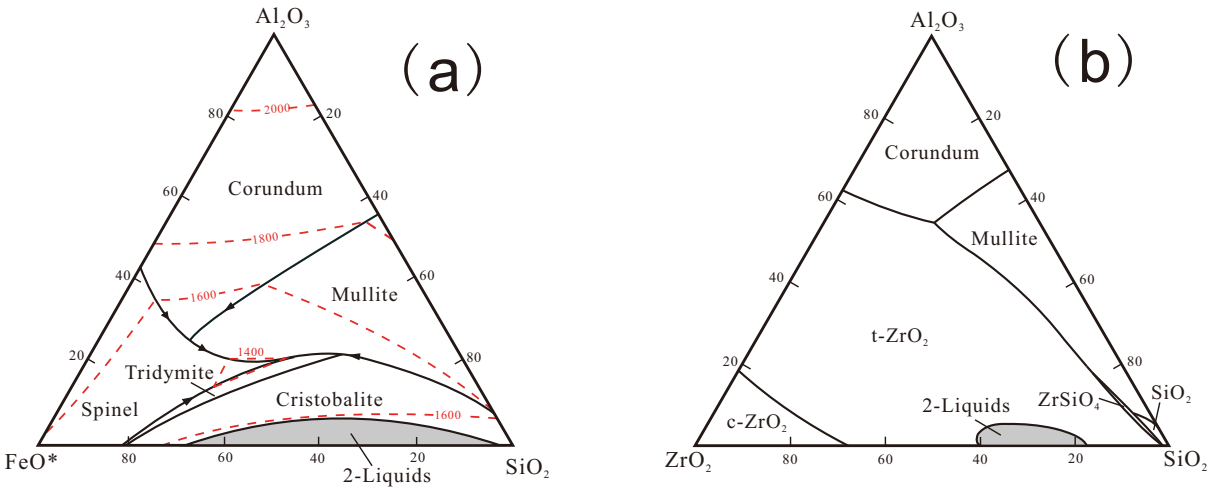

Fig. 7

This is the peer-reviewed, final accepted version for American Mineralogist, published by the Mineralogical Society of America.
The published version is subject to change. Cite as Authors (Year) Title. American Mineralogist, in press.
DOI: https://doi.org/10.2138/am-2020-7347. http://www.minsocam.org/

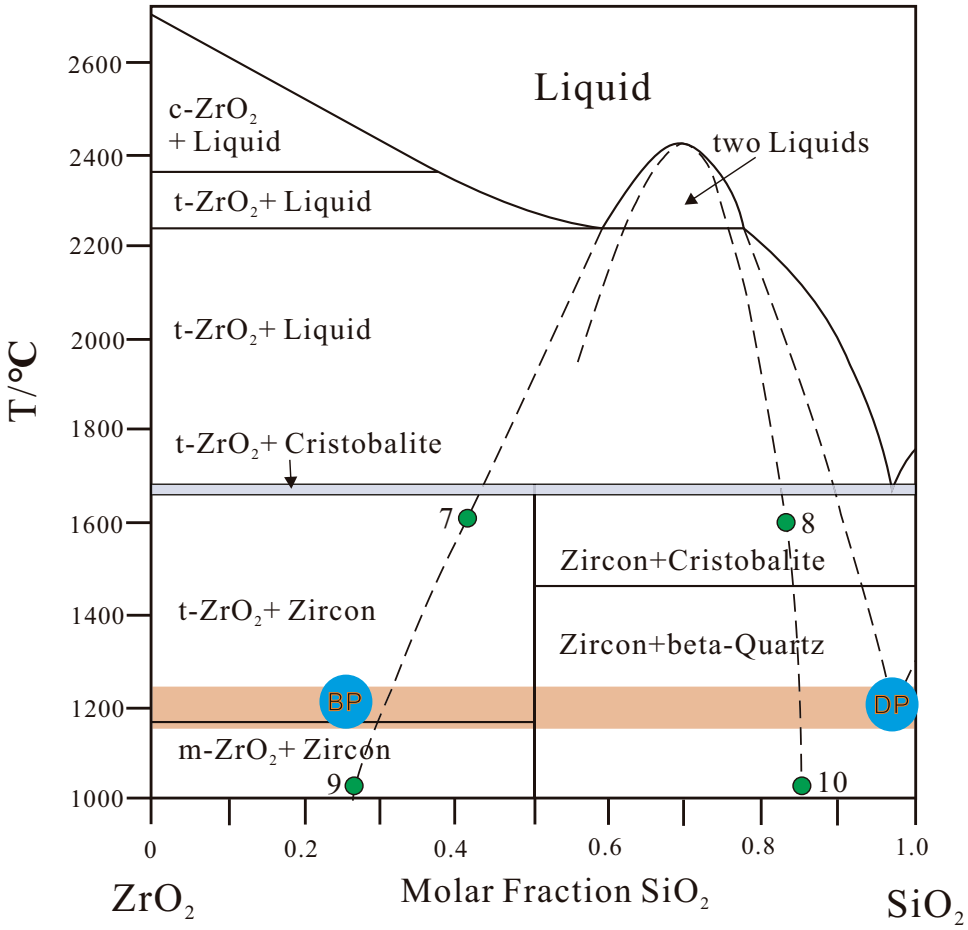

Fig. 8